Observational constraints to the dynamics of dust particles in the coma of comet 67P/Churyumov–Gerasimenko

E. Frattin [1]*, I. Bertini,[2,3] S. L. Ivanovski,[4] F. Marzari [1], M. Fulle [4], V. V. Zakharov,[2,3] F. Moreno,[5] G. Naletto [1], M. Lazzarin,[1] P. Cambianica,[6] G. Cremonese,[6] S. Ferrari,[7] F. Ferri,[7] C. Güttler,[8] F. La Forgia,[1,2] A. Lucchetti,[6] M. Pajola,[6] L. Penasa [7], A. Rotundi,[2,3] H. Sierks[8] and C. Tubiana [3,8]

[1]*Dipartimento di Fisica e Astronomia G.Galilei, Università di Padova, Vicolo dell'Osservatorio 3, I-35122 Padua, Italy*
[2]*Dipartimento di Scienze e Tecnologie, Università di Napoli 'Parthenope', CDN IC4, I-80143 Naples, Italy*
[3]*Institute for Space Astrophysics and Planetology (IAPS)-INAF, Via Fosso del Cavaliere 100, I-00133 Rome, Italy*
[4]*Osservatorio Astronomico di Trieste, Istituto Nazionale di Astrofisica, Via G.B. Tiepolo 11, I-34143 Trieste, Italy*
[5]*Instituto de Astrofísica de Andalucía, CSIC, E-18008 Granada, Spain*
[6]*Osservatorio Astronomico di Padova, Istituto Nazionale di Astrofisica, Vicolo dell'Osservatorio 5, I-35122 Padua, Italy*
[7]*Center of Studies and Activities for Space (CISAS) G. Colombo, University of Padova, Via Venezia 15, I-35131 Padua, Italy*
[8]*Max Planck Institute for Solar System Research, Justus-von-Liebig-Weg 3, D-37077 Göttingen, Germany*

ABSTRACT

In this work, we aim to characterize the dust motion in the inner coma of comet 67P/Churyumov–Gerasimenko to provide constraints for theoretical 3D coma models. The OSIRIS camera on-board the Rosetta mission was able for the first time to acquire images of single dust particles from inside the cometary coma, very close to the nucleus. We analyse a large number of particles, performing a significant statistic of their behaviour during the post-perihelion period, when the spacecraft covered distances from the nucleus ranging between 80 and 400 km. We describe the particle trajectories, investigating their orientation and finding highly radial motion with respect to the nucleus. Then, from the particle brightness profiles, we derive a particle rotational frequency of $\nu < 3.6$ Hz, revealing that they are slow rotators and do not undergo fragmentation. We use scattering models to compare the observed spectral radiance of the particles with the simulated ones in order to estimate their size, finding values that range from millimetres up to centimetres. The statistics performed in this paper provide useful parameters to constrain the cometary coma dynamical models.

Key words: methods: data analysis – techniques: image processing – techniques: photometric – comets: individual.

1 INTRODUCTION

The cometary coma is a complex environment where several physical and chemical processes regarding solid and gaseous materials emitted from the nucleus take place, such as fragmentation, sublimation, and photoionization. Many models of different levels of complexity have been developed during the years in order to describe the cometary dust motion (Crifo et al. 2005; Zakharov et al. 2009; Marschall et al. 2016; Ivanovski et al. 2017a). The main forces that govern the motion of the particles in the vicinity of the nucleus are the gravitational force exerted by the comet, the aerodynamical force generated by the gas drag, the solar gravity, and the solar radiation pressure.

The gas is considered to be the main driver of the motion up to a certain distance from the nucleus at which the dust particles reach their terminal velocity decouple from the gas, which occurs at about 10 nucleus radii from the centre of mass (Crifo et al. 2002, 2005; Zakharov et al. 2018). Fulle et al. (2015) and Ivanovski et al. (2017a) computed the exact distances where single particles reach

their terminal velocity for 67P/Churyumov–Gerasimenko (hereafter 67P), obtaining values that range between 10 and 100 km depending on the gas field, the mass, and density of the particles. The gas production rate governs the release process and it changes along the comet trajectory before and after perihelion.

In general, since drag and gravity decrease with the distance from the nucleus, at a certain height the solar pressure force finally dominates: this may happen either close or far from the nucleus, depending on the particular case (Moreno et al. 2017; Ivanovski et al. 2017a; Skorov et al. 2018).

Furthermore, the shape of the particles plays an important role in the dynamical models. The up-to-date observational data revealed limitations of the models which assume sphericity of dust grains. Indeed, the evidence of irregular shape of dust particles was revealed by the Stardust mission, by the Interplanetary Dust Particles (IDPs) analysis (Rotundi et al. 2007, 2008) and by the measurements obtained by the Grain Impact Analyzer and Dust Accumulator (GIADA, Colangeli et al. 2007; Della Corte et al. 2014) and Cometary Secondary Ion Mass Analyzer (COSIMA, Le Roy et al. 2015) for the Rosetta mission (Langevin et al. 2016; Fulle & Blum 2017; Ivanovski et al. 2017a). The images provided by the Optical, Spectroscopic, and Infrared Remote Imag-

* E-mail: elisa.frattin@unipd.it

Table 1. The dust model initial parameters used in this work.

Input parameter	Parameter value	Comments
	Particle parameters	
Particle size [m]	1.0×10^{-3}–1.0×10^{-1}	Observational constraint derived from this study
Particle density [kg/m^3]	800	Constrained by the GIADA data (Fulle et al. 2016a, 2017)
Spheroid aspect ratio, a/b	2/3 and 3/2	Observational constrain derived as the most relevant in this study
Initial particle orientation [deg]	22.5–67.5°	Compatible with the one used to reproduce particle speeds measured by GIADA (Ivanovski et al. 2017b)
Particle temperature, T_d [K]:	300	Fulle et al. (2020)
	67P/CG parameters	
Radius, R_N [m]	2.0×10^3	Sierks et al. (2015)
Mass, m_N [kg]	1.0×10^{13}	Pätzold et al. (2016)
Total gas production [mol s^{-1}]	10^{28}	Hansen et al. (2016)

ing System (OSIRIS, Keller et al. 2007) revealed indications of rotational motion of particles by the brightness variation in the tracks of single particles, interpreted as rotational motion of non-spherical particles (Fulle et al. 2015; Frattin et al. 2017). Therefore refined models, based on the use of aspherical particles, have been developed by Ivanovski et al. (2017a) and Skorov et al. (2016).

All the aforementioned models dealing with dust dynamics in the inner coma need to be verified, tested, and refined through observational data. It is therefore of pivotal importance to use Rosetta data to constrain theoretical interpretations providing inputs to the models. During orbiting around comet 67P, the OSIRIS camera onboard the Rosetta spacecraft (Keller et al. 2007) was able to acquire images from inside the cometary coma, close to the nucleus. In 2015 July–2016 January time frame, the spacecraft was at distances between 80 and 400 km from the nucleus (with one configuration at 1200 km). For the first time, it was possible to directly observe tracks of single dust particles and measure their light curve, to determine hints on their rotational state, and size, providing a good statistics of the aforementioned parameters, due to the huge amount of data collected.

In this work, we present an extensive analysis of dust particles characteristics and dynamics. In Section 2, we describe the data set. In Section 3, we show the observational evidence of the radial motion of the dust particles; in Section 4, we present a statistic of the rotational frequency of the particles in the inner coma of the comet. Afterwards, we give an estimate of their shape evaluating their flattening. In Section 5, we provide a photometric analysis of the dust particles deriving their size. A description of the rotational dynamics of the dust is given in Section 6. The conclusions are given in Section 7.

2 DATA

To study the direction of motion and the rotational state of the particles we used images acquired from 2015 August to 2016 January (the perihelion passage was in 2015 August) by the OSIRIS Narrow Angle Camera (NAC) in the Orange filter ($\lambda = 649$ nm), with an exposure time of 12.5 s.

For the analysis we used 92 radiometric calibrated and geometric distortion corrected OSIRIS Level 3 and 3B (CODMAC L4) images.[1] Details about the data processing, including all calibration steps

[1]The data are available at the Planetary Science Archive of the European Space Agency under https://www.cosmos.esa.int/web/psa/rosetta

applied to the images, can be found in Tubiana et al. (2015). The only difference between the used image levels is solely the unit: OSIRIS Level 3 images are in W/(m^2 sr nm), while L3B images are I/F, thus unity.

During the entire mission, we regularly acquired sequences of images named dust particle track and dust particle colour, which were designed to study the motion and the colours, respectively, of individual particles in the dust coma. The design of those sequences was the same thorough the mission, allowing to combine data acquired at different epochs.

In this work, we analyse both type of sequences. The activity name of each sequence is listed in Tables 2 and 3. At the time of the observations, the Rosetta spacecraft was at a distance from the nucleus between 84 and 437 km. The Rosetta + Z-axis, which is aligned with the camera boresight direction, was off-pointing with respect to the nucleus, which is therefore outside the camera field of view. To study the direction of the dust motion, in Section 3, we have analysed 28 images belonging to five sets of images listed in Table 1. The nucleus phase angle α (i.e. the angle between the direction of Sun and the direction of spacecraft as seen by the nucleus) is reported here for geometrical purposes and in these images is always less than 90°, hence the spacecraft is located in the day side of the coma, see Fig. 1.

The plane of sight is perpendicular to the plane defined by the Sun, the nucleus, and the spacecraft and these planes intersect at the line given by the direction between the Sun and the spacecraft. Therefore, the plane of sight contains the Sun. The images elongation ϵ (i.e. the angle between the direction of the line of sight and the direction of the Sun as seen by the spacecraft) changes within the sequence from the solar direction towards the antisolar direction, from 50° to 160°. It means that the camera points dust that scatters from the forward direction up to the backward direction with respect to the Sun. This allows to investigate different parts of the coma at the same epoch. The phase angle of the dust follows the relation $\alpha_{\text{dust}} = 180° - \epsilon$.

To study the rotational state and the photometry of the dust particles, in Sections 4 and 5, we have analysed 64 images belonging to seven sets of images taken in various epochs, listed in Table 3. We decided to focus on sets of images where the observational geometry configuration formed by the spacecraft, the comet, and the Sun remained constant. This means that the phase angle α, the elongation of the Sun ϵ, and the angle γ (i.e. the angle between the direction of the spacecraft and the direction of the line of sight) are fixed within the observational series, see Fig. 2. In this way, the condition of illumination of the particles during the time interval of a series is the same.
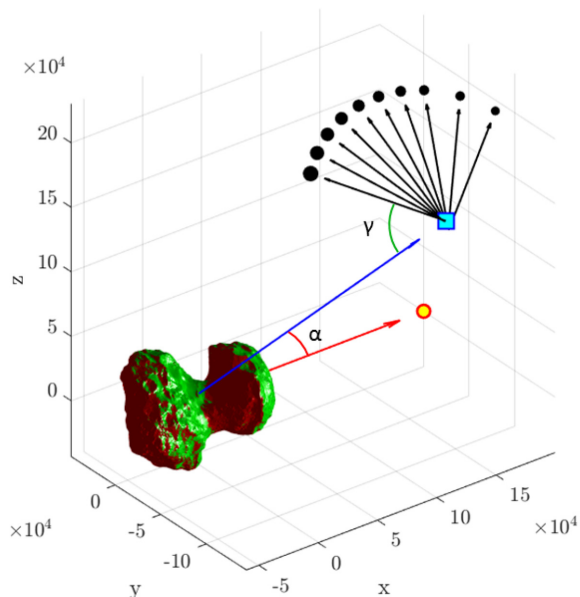
Figure 1. Example of the observational configuration of the set of images described in Table 2, the case of STP 081 GRAIN_COLOR_002. The red arrow represents the direction of the Sun (yellow circle). The black arrow represents the line of sight of the camera (cyan square) for each image, and the black circles stand for the dust particles. The line of sight lies on a plane perpendicular to the plane containing the Sun, the comet, and the s/c.
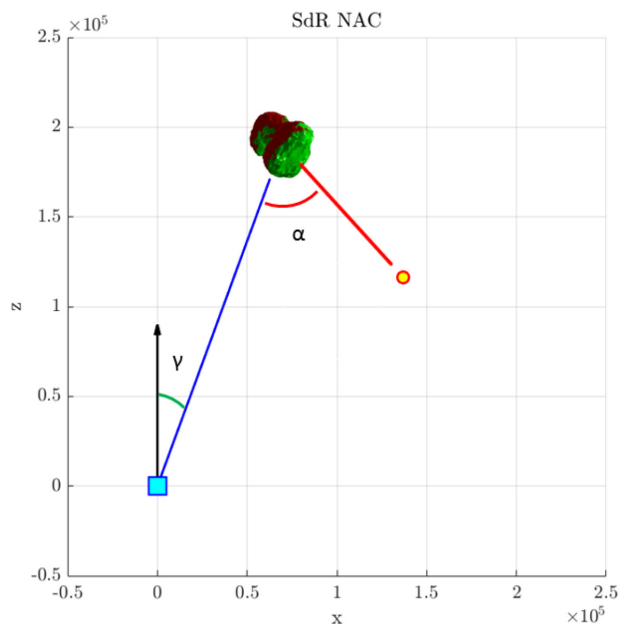

Figure 2. Example of the observational configuration of the set of images described in Table 3, the case of STP 081 GRAIN_TRACK_003. The red arrow represents the direction of the Sun (yellow circle). The black arrows represent the line of sight of the camera (cyan square). The line of sight lies on the plane containing the Sun, the comet, and the s/c.

2.1 Detection method

The OSIRIS NAC camera is able to observe single dust particles in the coma of 67P. Each particle draws a track on the plane of the image, due to its motion during the exposure time. Therefore, the track is the 2D projection on the CCD focal plane of the 3D particle
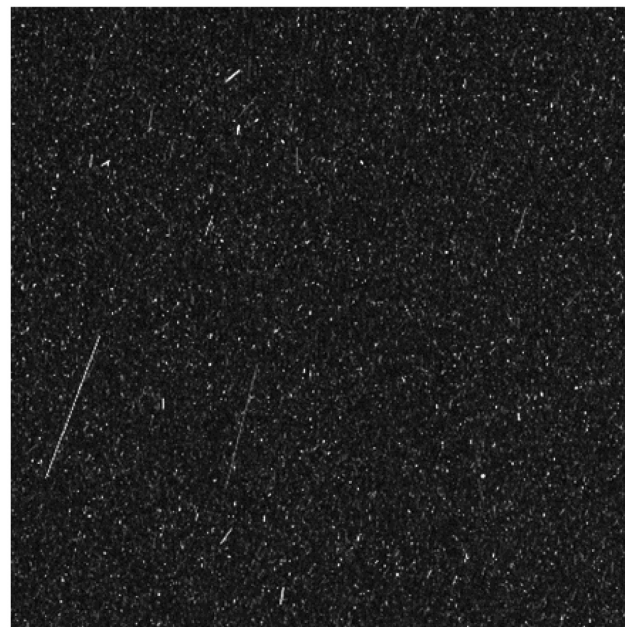

Figure 3. Image taken by NAC on 2015 November 30 at UT 19:25:04.078, belonging to STP 084. The colour scale follows a square root variation. The grey scale goes from black to white, which correspond to flux values of 0 and 0.000185 W/(m^2 nm sr), respectively. The size of the image is 440 × 440 px.
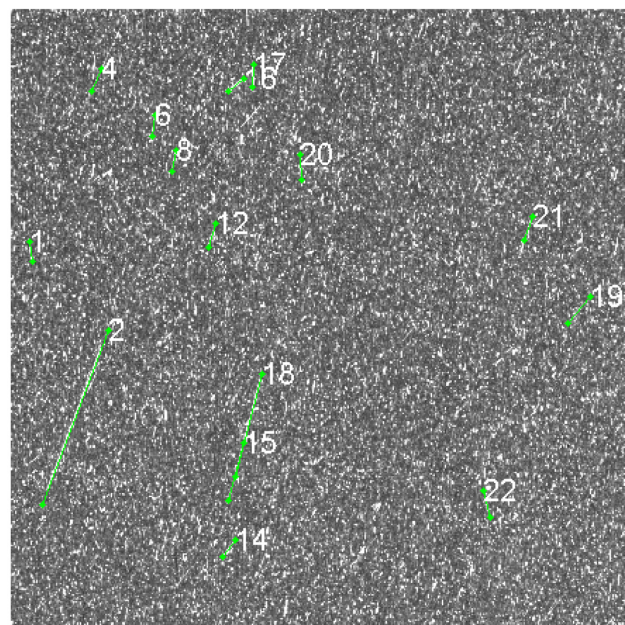

Figure 4. Last step of the detection process on image taken by NAC on 2015 November 30 at UT 19:25:04.078. The tracks are identified with a number and highlighted in green. The colour scale follows a square root variation.

motion. We use the automatic method developed by Frattin et al. (2017) to detect the tracks from the images and to provide some photometric and geometric parameters, as their radiance, full width at half-maximum (FWHM), and orientation.

Fig. 3 shows an example of an OSIRIS image with dust tracks, while Fig. 4 illustrates the final step of the detection process in which the tracks are identified with a green line and a number. The method is based on a similarity function that evaluate the

Table 2. OSIRIS data set used in Section 3 to measure the particles direction of motion and their alignment with nucleus and Sun directions. MTP: medium time planning of the data set. STP: short time planning of the data set. Activity: the activity name of the sequence. Epoch: image acquisition day. Start time: image initial acquisition time. Δt: range of time between the first and last image acquisition. r_c: nucleocentric distance. r_h: heliocentric distance. α : phase angle as shown in Fig. 1 (i.e. angle between spacecraft and Sun as seen by the comet). ϵ: elongation of the Sun (i.e. angle between the camera pointing direction and the Sun as seen by the s/c). The exposure time of each image is 12.5 s.

MTP	STP	Activity	Epoch	Start time	Δt(hh mm ss)	r_c(km)	r_h(au)	$\alpha(°)$	$\epsilon(°)$
021	075	GRAIN_COLOR_002	2015.09.28	14:42:32.150	01.04.00	1220	1.37	50	90–160
021	078	GRAIN_COLOR_004	2015.10.18	02:51:30.857	01.28.00	437	1.47	65	70–150
022	079	GRAIN_COLOR_001	2015.10.23	20:04:28.191	01.28.00	389	1.51	63	70–130
022	081	GRAIN_COLOR_002	2015.11.06	20:05:59.163	01.31.00	244	1.61	63	55–140
023	083	GRAIN_COLOR_001	2015.11.19	13:11:24.629	01.36.00	126	1.70	74	50–130

correspondence between two images. A set of synthetic tracks is generated, characterized by their orientation and FWHM, given by the convolution of a rectangular function with a bi-dimensional Gaussian. Then, the Normalized Cross Correlation allows to evaluate the similarity between the features identified on a local zone of the images and the synthetic tracks generated. Eventually the length of the tracks, their position, orientation, flux, and FWHM are provided. The flux is computed subtracting the background which is evaluated considering a rectangular area around the track, with sides parallel to the sides of the image and with length and height 10 pixel longer than the projection of the track on the two dimensions, in order to include the track properly.

3 TRANSLATIONAL MOTION OF THE DUST

In this section, we study the translational motion of the dust in the inner coma of comet 67P. We measure the particles direction of motion and we compare it with the trajectories computed by an appropriate dynamical model, in order to describe the inner coma dust motion. The data set consists of the post-perihelion images reported in Table 2; geometry is described in Section 2.

3.1 Method

To measure the direction of motion of the dust particles we evaluate the angles shown in Fig. 5. The angle δ is defined between the velocity vector of the particle on the plane of the image (defined by the track itself) and the projected position vector of the nucleus on the plane of the image, in the NAC reference system, while the angle β is defined between the projection of the velocity vector of the particle on the plane of the image, and the projected position vector of the Sun.

The positions of the Sun and of the nucleus are derived using the SPICE Kernels (Acton 1996) and eventually, the cosine of the angles δ and β are computed. It is important to notice that the observational configuration changes within a single set of images. The elongation varies so the region of the coma investigated changes too.

3.2 Measurements

We measure the direction of motion of the particles observed in the images taken in the post-perihelion period ranging from 2015 September to November. The results for the set STP 075 are shown in Fig. 6. The results for the other set of images are reported in Appendix A (Figs. A1–A4). Each histogram represents the values of the cosine of the angle δ that each particle detected in a single image forms with the nucleus position vector. The elongation (ϵ) changes within a set, following the values illustrated in Table 2.

When the value of $\cos(\delta)$ is close to 1, the particle track, representing the projection of the motion on the plane of the image, is almost parallel to the direction vector of the nucleus. Our analysis shows that the majority of the particles have a value of $\cos(\delta)$ very close to 1, proving that the dust motion is mainly radial to the nucleus. Therefore, the bulk of dust aggregates comes directly from the nucleus, while the small deviations are probably generated by a population of dust inbound orbits around the nucleus (Bertini et al. 2019).

3.3 Model

We developed a simple model of dust dynamics in the region where dust is completely decoupled from the gas. It is assumed that at the entrance in this region the dust particles have some initial velocity and further their motion is governed by the solar gravitational force, the solar radiation pressure and the nucleus gravitational force.

We consider a static model in which the heliocentric distance of the nucleus and of the spacecraft are constant, justified by the short interval of time (h) with respect to the heliocentric motion of the
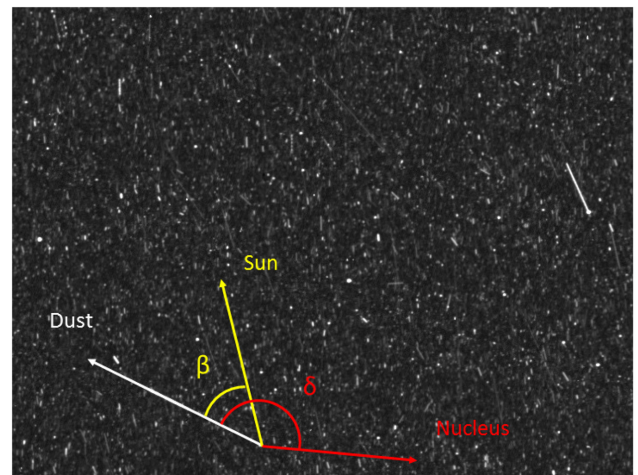

Figure 5. Single NAC image taken on 2015 November 30, STP 084, at UT 18:51:43.22. The image shows the construction of the position vectors used to compute the direction of motion of the dust. The track generated by the passage of a dust particle in the coma is shown in white, the unit vector of the position of the Sun in yellow and the unit vector of the position of the nucleus in red. The colour scale follows a square root variation. The grey scale goes from black to white, which correspond to flux values of 0 and 0.000035 W/(m² nm sr), respectively. The size of the image is 722 × 541 px.
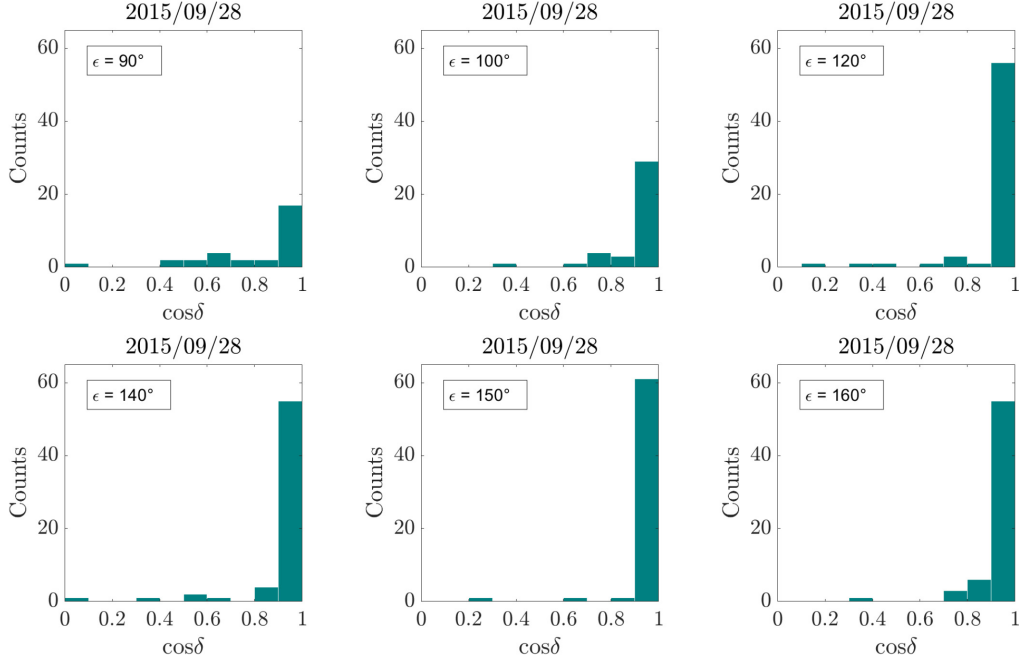
Figure 6. The histograms show the value of the cosine of the angle δ between the velocity vector of the particle on the image plane, and the projected position vector of the nucleus on the plane of the image, in the NAC reference system, for the set STP 075 GRAIN_COLOR_002.

comet in which the ejection events occurred. The distance between the spacecraft and the nucleus is also constant.

The gravitational force of the Sun is defined as follows:

$$F_{G\odot} = \frac{GM_\odot}{r_\odot^2} m_p \qquad (1)$$

where $m_p = \frac{4\pi\rho_d r^3}{3}$ is the mass of the particle, ρ_d is the density of the particle, and r the radius. $r_\odot = (1.496 \times 10^{11} r_h)$ is the heliocentric distance in metres.

The radiation pressure is

$$F_{\rm rad} = \frac{F_\odot}{r_h^2} \frac{Q_{\rm pr} \pi r^2}{c}, \qquad (2)$$

where $F_\odot$ is the Sun radiation intensity at 1 au (corresponding to $F_\odot = 1360 \, \mathrm{W \, m^{-2}}$), c is the speed of light, and $Q_{\rm pr}$ is the scattering efficiency for radiation pressure ($Q_{\rm pr} = 1$ for total reflecting particles).

The gravitational force of the nucleus is

$$F_{\rm g} = \frac{GM_N}{r_c^2} m_p, \qquad (3)$$

where $M_N = 10^{13}$ kg is the mass of the nucleus (Pätzold et al. 2016), and r_c is the distance of the particle from the nucleus.

We simulate an initial momentum spread isotropically from 10 km from the surface of the nucleus, which is the distance at which the drag force becomes negligible. The velocity is defined in the nucleus reference system as:

$$\begin{cases} v'_x = v_0 \sin\theta \cos\phi, \\ v'_y = v_0 \sin\theta \sin\phi, \\ v'_z = v_0 \cos\theta \end{cases}$$

where v_0 is the initial velocity value, $\theta \in [0, \pi]$ is the polar angle, and $\phi \in [0, 2\pi]$ is the azimuthal angle.

We compute the trajectories travelled by dust particles of radius ranging from 0.1 to 10 mm. The model depends on the density of the

dust ρ_d, the distance from the Sun r_h, and the initial velocity vector v_0.

We set $\rho_d = 800 \, \mathrm{kg \, m^{-3}}$ (Fulle et al. 2016b) and $r_h = 1.37$ au as in the case of the set of images STP 075 taken just after the perihelion.

The initial velocity is v = 20, 5, and 1.5 m s^{-1}, respectively, for particles of 0.1, 1, and 10 mm, based on GIADA and OSIRS measurements of Della Corte et al. (2016) and Ott et al. (2017) and on the work of Ivanovski et al. (2017a). We note that the dust velocity may depend on the direction from where the particle comes. Therefore, in our simple model with isotropic ejection of particles, we use some averaged velocities. The dust particles undergo the solar radiation pressure in different ways, depending on their size and mass. The smaller the particle the stronger the effect of the solar radiation pressure. At the same time, the small particles have higher initial velocities (due to acceleration by the gas). The combination of these parameters result in an almost radial motion of all particle size ranges considered. Fig. 7 shows the 3D trajectories of the particles of 0.1 mm in green, of 1 mm in blue, and of 10 mm in red. The Sun lies on the negative branch of the x-axis and the nucleus of 67P is located at the origin of the axis. The black symbols represent the position of the s/c in the five epochs. The plane in which the camera is pointing is always perpendicular to the plane formed by the Sun, the nucleus, and the spacecraft. Following this model, we find that the motion is almost radial in the inner part of the coma of the comet 67P for this range of particle sizes and initial velocities.

4 ROTATIONAL STATE OF DUST PARTICLES

In this section, we present the analysis performed on particles that show evidence of rotation. We refer to the data set of Table 3. First, we measure the rotational frequency of the particles, then we evaluate their flattening, giving some information about their shape.
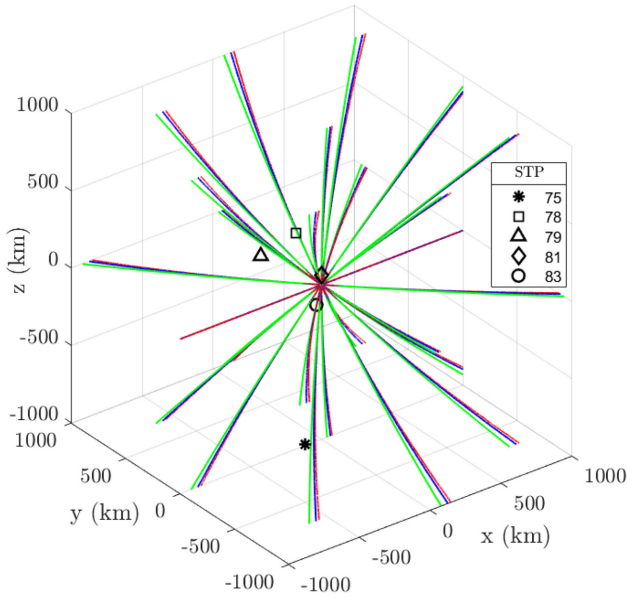
Figure 7. The figure shows the 3D trajectories of the dust particles ejected from the nucleus in all direction isotropically. The colour code is the following: green for particles of 0.1 mm and $v = 20 \, \mathrm{m \, s^{-1}}$, blue for particles of 1 mm and $v = 5 \, \mathrm{m \, s^{-1}}$, and red for particles of 10 mm and $v = 1.5 \, \mathrm{m \, s^{-1}}$. Also the s/c position at each STP is shown.

4.1 Method

We observe that some tracks show periodic variations in brightness, interpreted as rotational motion of the single dust particle. Fig. 8 shows an example of light curve of a rotating particle. As a comparison, Fig. 9 shows a light profile with irregular radiance variations below the level of the background that cannot be considered as evidence of rotation. We evaluate each track to distinguish between rotating particles and those that do not show evidence of rotation. We assume ellipsoidal particles with uniaxial rotation. We consider the three rotational modes around the main axis both for the prolate and oblate particles. Depending on the modes of rotation the track generated by the passage of the particle in the field of view shows brightness variation or not. For instance, an oblate spheroid rotating around its major axis perpendicular to the line of sight generates two peaks of brightness at each rotation, while if it rotates around its minor axis or around it major axis but parallel to the line of sight, it generates a homogeneous track. Consequently, the latter cannot provide information about the particles shape. We use a criterion to classify the particles as rotating or not: the amplitude between the maximum and the minimum signal must be larger than the background signal. We discard those tracks that show only two peaks of brightness, in order to avoid possible contamination from two different tracks (Fulle et al. 2015). Overall, we detect 1916 particles of which 344 show a periodical light curve that corresponds to 18 per cent of the whole population.

4.2 Rotational frequency

In approximation of uniaxial rotation of ellipsoidal particles with smooth homogeneous surface, the rotational frequency is straightforwardly computed dividing the number of maximum brightness peaks in the light curves for the exposure time. It does not depend on the track length, neither on the track distance nor the radiance, but only on the number of peaks. Hereafter the rotational frequency

refers to the brightness frequency. Nevertheless, the statistics are affected by a bias due to the fact that only the longest tracks can provide fast rotations. Therefore, in order not to underestimate the high frequencies, we weight each track by its length, following Fulle et al. (2015). The probability of obtaining a specific rotational frequency is given by the formula $p_n = f_n \cdot l_n / \sum_{i=1}^{N} l_i$, where f_n is the rotational frequency of the particle, l_n is the length of the track, and N is the total number of tracks in the image. In Fig. 10, the length-frequency parameter space is shown. Furthermore, we correct for the projection effect. Since the trajectories are almost radial, as shown in the previous section, we can approximate the angle they form with the line of sight to the angle γ shown in Table 3. Therefore, the final length of a track (l_n) is equal to the length observed divided by the sine of the angle gamma. In Fig. 11, we report the distribution of the rotational frequencies weighted for the length of the tracks for the entire sample of particles detected in every single daily set.

All the image sets show a higher probability to find slow rotating particles rather than fast ones. Moreover, the decreasing trend is common to all sets of images taken at different epochs and at different nucleocentric distances. This suggests that we are looking at a population of dust particles that did not undergo significant morphological and dimensional changes after their ejection from the nucleus. Therefore, a cumulative study of the data is allowed.

In Fig. 12, the distribution of the rotational frequencies of the whole set of images is merged in one single histogram. It results in a clear decreasing trend from 0.4 ± 0.2 up to a maximum of 3.6 ± 0.2 Hz, where the uncertainty corresponds to the bin sensitivity. About 40 per cent of the particles have frequencies between the minimum value of 0.24 Hz (corresponding to three peaks of brightness) and 0.56 Hz (corresponding to seven peaks of brightness).

These values are in agreement with the ones obtained by Fulle et al. (2015) who found a comparable decreasing trend of the rotational frequency during the pre-perihelion period. This trend lets us suppose that the majority of the particles lies on the very left part of the histogram, which cannot be examined since the limited exposure time of our sample can only provide rotational frequencies above the minimum value of 0.24 Hz. Slower frequencies can be investigated looking at images with longer exposure time. Therefore, we expect that the particles do not rotate very fast in the inner coma, excluding a massive effect of fragmentation driven by their rotational motion. Overall, the tracks that show brightness variation are a percentage that range between 11 and 46 per cent of the average number of tracks observed in a single image (see Table 3). Therefore, all tracks without brightness variation could be representative of either very slow rotators, with periods larger than the exposure time of the image, or particles that are rotating exposing always the same face.

4.3 Flattening

The morphology of the dust of the order of hundreds of microns in 67P's coma was revealed by the images of the Micro-Imaging Dust Analysis System (MIDAS, Riedler et al. 2007) and COSIMA (Langevin et al. 2016; Mannel et al. 2016). The dust particles show irregular shapes; they can be either fluffy aggregates or compact particles (Güttler et al. 2019). To give an estimate of their flattening, we evaluate the aspect ratio of particles via measurements of the maximum to minimum brightness ratio of the light curves, which represents the projected area of the aggregates on the plane of the image assuming uniaxial rotation and homogeneous composition. We decide to approximate these shapes with an ellipsoid of revolution, i.e. spheroid, which represents, as a first approximation, an irregular

Table 3. OSIRIS data set used in Section 4 for the analysis of dust rotational motion. MTP: medium time planning of data acquisition. STP: short time planning of data acquisition. Activity: the activity name of the sequence. Epoch: image acquisition day. Start time: image initial acquisition time. Δt: range of time between the first and last image acquisition. r_c: nucleocentric distance. r_h: heliocentric distance. α: phase angle as shown in Fig. 2. ϵ: elongation of the Sun (i.e. angle between the camera pointing direction and the Sun as seen by the s/c). γ: angle between the comet and the pointing direction as seen by the s/c. #rot: number of rotating particles individuated in each data set. #im: number of images analysed for each data set. #tot: total number of particles in the data set. %rot: percentage of rotating particles with respect to the total. f: average mode of the rotating frequency. a/b: average aspect ratio of the particles as defined in Section 4.3. bkg: value of the background averaged over each data set in W/(m² nm sr), computed on an area of 30 pixel radius of each image. Since the illumination condition is fixed the background variation among each data set is negligible. The exposure time of each image is 12.5 s.

| MTP	STP	Activity	Epoch	Start time	Δt (hh mm ss)	r_c(km)	r_h(AU)	α(°)	ϵ(°)	γ(°)	#rot	#im	# tot	%rot	f(Hz)	a/b	bkg
019	067	GRAIN_COLOR_002	2015.08.04	14:20:31.208	01.15.19	238	1.25	90	135	45	89	8	599	25	0.4	1.5	3×10^{-7}
022	081	GRAIN_TRACK_003	2015.11.10	13:32:44.361	03.30.01	202	1.61	62	137	19	43	12	284	22	0.4	1.5	2×10^{-7}
023	083	GRAIN_TRACK_001	2015.11.20	18:29:26.800	03.20.01	142	1.70	87	122	29	70	6	355	30	0.4	1.9	2×10^{-7}
023	084	GRAIN_TRACK_002	2015.11.30	17:56:25.051	02.20.01	111	1.70	90	120	30	9	7	107	11	0.4	1.1	1×10^{-7}
023	086	GRAIN_TRACK_003	2015.12.10	17:32:23.417	03.50.00	99	1.86	89	76	−15	74	10	301	41	0.8	2.4	4×10^{-7}
024	087	GRAIN_TRACK_001	2015.12.17	01:53:01.775	04.30.00	100	1.9	90	106	16	50	12	198	46	0.4	1.3	1×10^{-7}
024	090	GRAIN_TRACK_003	2016.01.06	11:13:43.828	02.40.00	84	2.06	90	75	−15	13	9	72	38	1.6	1.6	2×10^{-7}
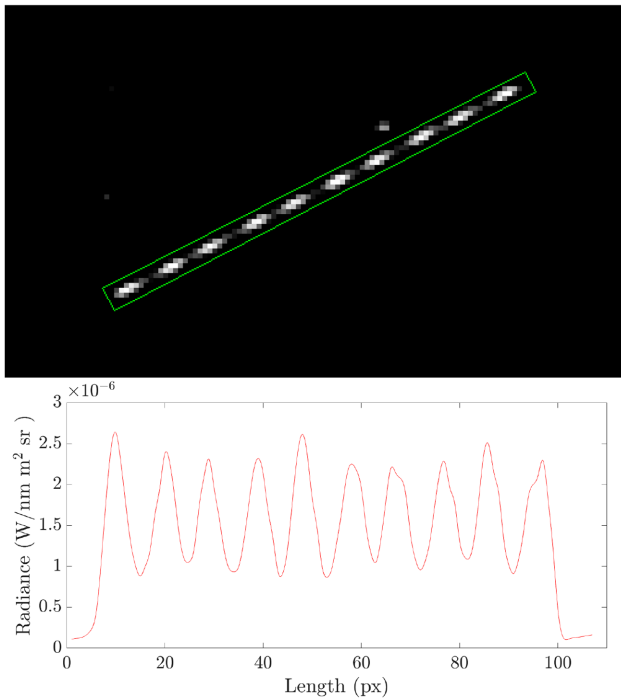
Figure 8. A rotating particle extracted from a single NAC image taken on 2015 December 15, STP 087, at UT 01:51:40.319 (top panel) and its brightness profile (bottom panel). The size of the image is 120×70 px.

Figure 9. A particle that does not show evidence of rotation extracted from a single NAC image taken on 2015 December 17, STP 087, at UT 02:31:40.068 (top panel) and its brightness profile (bottom panel). The size of the image is 100×50 px.

aggregate with two main cross-sections on the plane of the image. Spheroids are also used as dust shape models by Fulle et al. (2015), Ivanovski et al. (2017a,b), and Moreno et al. (2018) to represent the dynamics of the dust in the coma. The estimated aspect ratios are always larger than 1 (which is the value for a sphere), because we cannot discriminate between oblate and prolate spheroids. It means that a value equal to 2, for instance, could be attributed to a prolate spheroid but also to an oblate spheroid with aspect ratio 0.5. In Fig. 13, the distribution of the aspect ratio values of the whole sample of particles is shown. The majority of the population lies between 1.1, for almost spherical particles, and 2. Nevertheless, the aspect ratio reaches values up to 11, revealing that the particles might be also very elongated (Fulle et al. 2017).

Following the results of Fulle et al. (2015) we might suppose a higher percentage of oblate spheroids rather than prolate. Ivanovski
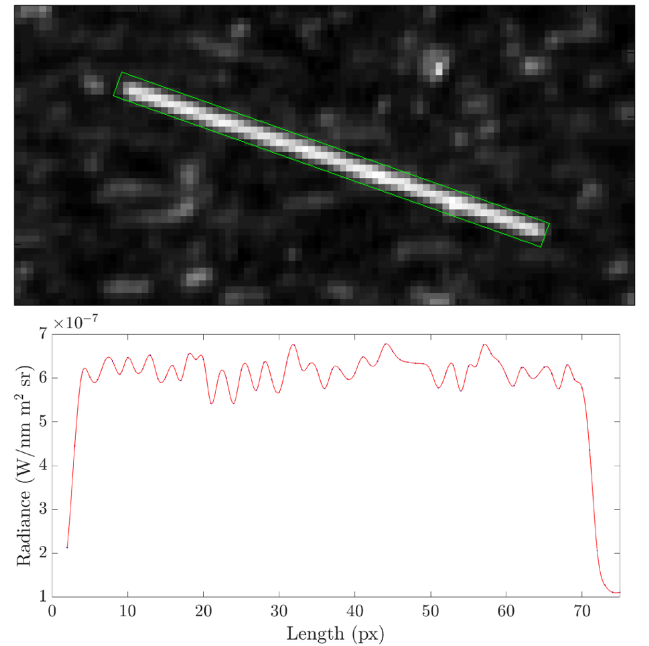
et al. (2017b) also found that oblate-like particles are the best candidates to reproduce GIADA data before perihelion. Muñoz et al. (2020) show that porous particles of an oblate-like shape oriented with its largest area facing the laser beam are necessary to reproduce the minimum of the OSIRIS phase functions at a phase angle of about 100 deg, as observed by Bertini et al. (2017).

In Fig. 14, we show the rotational frequency as a function of aspect ratio. The majority of the particles fill homogeneously an area defined by values of aspect ratio between 1 and 2 and with frequency between 0.24 and 0.56 Hz. Therefore, for those particles, it is not possible to infer a relation between rotational frequency and shape. Furthermore, we recognize two populations that deviate from the majority: one with high rotational frequency and low values of aspect ratio so more spherical particle, and the other with high values of aspect ratio, up to about 11, which corresponds to very elongated particles with relatively slow rotational frequency. Indeed more elongated
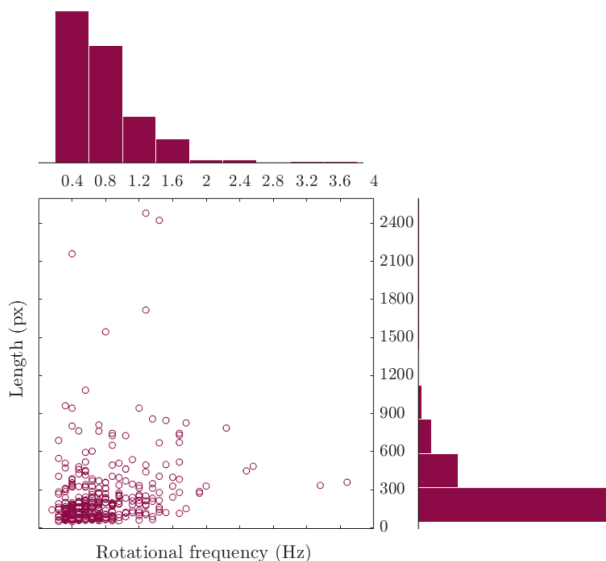
Figure 10. The figure shows the distribution of the particles in the parameter space defined by the tracks length (in px) and the rotational frequencies with their respective histograms.

particles are expected to rotate slower than the spherical ones, and this is linked to their inertia momenta (Ivanovski et al. 2017b). So, if the majority of the population is composed by slow rotators we might expect more aggregates with high elongation.

5 PHOTOMETRY

In this section, we measure the photometry of the particles in the images taken in the period 2015 August–2016 January (see Table 3). Then, we simulate the expected spectral radiances of the dust particles in the cometary coma with a scattering model. We compute the radiance of the single particles, changing a wide range of parameters such as the composition, size, heliocentric distance, and spacecraft distance. Finally, we compare them with the particles spectral radiances obtained directly from the images to estimate their size.

5.1 Scattering simulations

We use a scattering code in order to synthetically reproduce the photometry of the dust particles.

It takes into account a wide range of parameters such as the distance from the spacecraft and the Sun, the size of the particles, their phase angle, density, and the type of material they are made of, evaluated through the refractive index.

The code computes the amount of light scattered by each dust particle towards the CCD by using the Mie theory for spherical particles (Wolf & Voshchinnikov 2004). The software is optimized to consider arbitrary large size parameters and to give a first estimate of the particles size. Input parameters of the code are the phase angle of the dust, the density, and the refractive index of the material. We fix the phase angle at 90 deg and the density at 800 $kg\,m^{-3}$ (Fulle et al. 2016b). We select two characteristic compositions of the dust particles represented by the silicates, with refractive index m = 1.6 + $i10^{-5}$ (Muñoz et al. 2000; Frattin et al. 2019), and by the organics, with refractive index m = 1.3 + $i10^{-2}$ (Frattin et al. 2019).

This choice is based on the observations of the 67P dust provided by the instruments on-board the Rosetta s/c. COSIMA mass

spectrometer has confirmed the presence of abundant high-molecular weight organic matter, nearly 50 per cent in mass (Bardyn et al. 2017; Fray et al. 2017). Half of the mass of each dust particle consists of carbonaceous material with a mainly macromolecular organic structure; the other half being mostly composed of non-hydrated silicate minerals. GIADA has found that the measured densities of the 67P pebbles are consistent with a mixture of (15 ± 6) per cent of ices, (5 ± 2) per cent of Fe-sulphides, (28 ± 5) per cent of silicates, and (52 ± 12) per cent of hydrocarbons, in average volume abundances (Fulle et al. 2016b, 2017). Frattin et al. (2017) have found hints on the presence of three major groups of dust particles, based on the analysis of their spectral slope in the range [535–882] nm obtained from OSIRIS images. They found that the steepest spectra may be related with organic material, the spectra with an intermediate slope, can be a mixture of silicates and organics and the flat spectra may be associated with a high abundance of water ice (Frattin et al. 2017). Following these results, organics and silicates seem to be good representatives of the dust particles composition in the coma of 67P.

In Table B1, we report the expected spectral radiances for different combinations of the code parameters. We simulate particles with a size of 0.1, 1, 10 mm, at distance from the spacecraft that ranges from 1 to 20 km, following the results shown in Fig. 15. We fix the heliocentric distance at 1.3, 1.7, and 2.0 au to best represent the observations. The resulting spectral radiances have values between 10^{-3} and 10^{-10} W/(m² nm sr). They are strongly dependent on the heliocentric distance, showing the highest values at perihelion and decreasing as the comet moves away from the Sun, and are brighter for silicate particles than for the organic ones.

5.2 Results

We perform the photometry of the rotating dust particles analysed in the previous section and reported in the data set of Table 3. We evaluate the radiances of the whole track computing the sum of the signal of each pixel divided by the exposure time. In Fig. 16, we see the distribution of the particle spectral radiances for each epoch. The values range between 10^{-6} and 10^{-3} W/(m² nm sr), but the large majority is between 10^{-5} and 10^{-4} W/(m² nm sr). The uncertainty associated with the radiometric calibration is less than 1 per cent (Tubiana et al. 2015).

In order to give an estimate of the effective size (based on brightness) of the aggregates, we compared them with the simulated values. For the calibration, we use the data of Ott et al. (2017). We choose two aggregates at about 3–4 km from the spacecraft, at 1.25 au from the Sun, with a cm-size as a reference (precisely numbers 8 and 9 of their table 3). We find that the values of the spectral radiance, corrected for the phase function (Bertini et al. 2017), are, respectively, of $7.02 \pm 0.02 \times 10^{-4}$ and $5.15 \pm 0.02 \times 10^{-4}$ W/(m² nm sr), where the uncertainty is the standard deviation of the background. These results are strongly compatible with the simulations, whether we consider either organics or silicates. As a result, we find that the most populated values of spectral radiance correspond to mm and cm-size. The faintest value of radiance might be compatible with a particle size of the order of 0.1 mm (if very close to the s/c, i.e. 1 km) in both the cases of silicates and organics. Simulated particles smaller than mm have spectral radiances fainter than 10^{-7} W/(m² nm sr), a value that is outside the range obtained in the observations. Therefore, our analysis of rotational particles suggests that the majority of the dust aggregates we observe might likely have sizes that range from mm to cm.
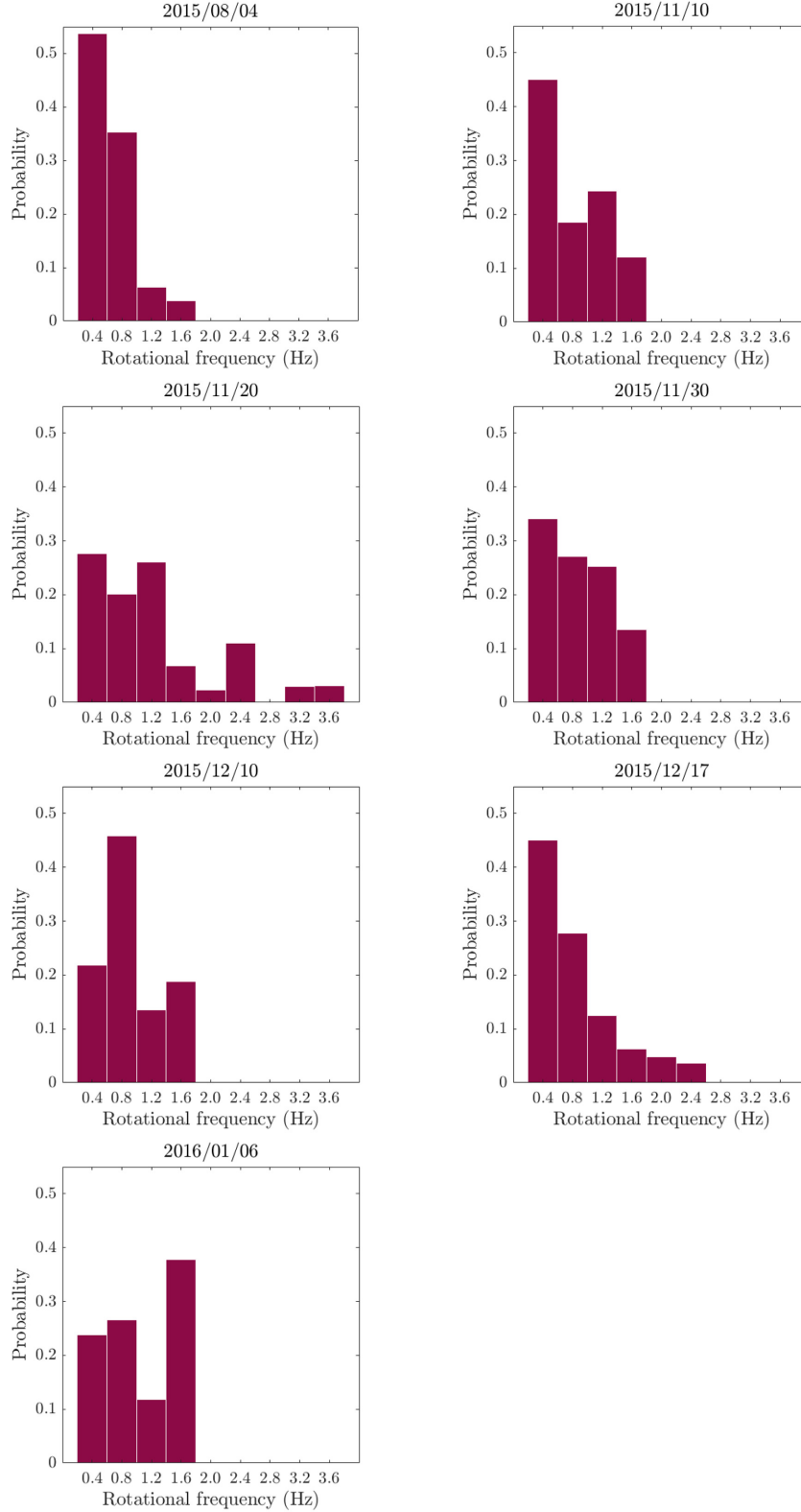
Figure 11. The histograms represent the rotational frequency distribution of the particles detected in the images listed in Table 3.

5.3 Particles distance and size

We estimate the minimum size of the observed rotating particles, based on the radiance computed with the scattering model. The faintest measured spectral radiance has value equal to 3×10^{-6}

W/(m^2 nm sr). We use the results of the scattering model to determine the minimum possible size corresponding to this radiance. To do this we set the heliocentric distance and the spacecraft distance of the particles at their minimum values, respectively, $r_h = 1.3$ au and $d_{s/c}$
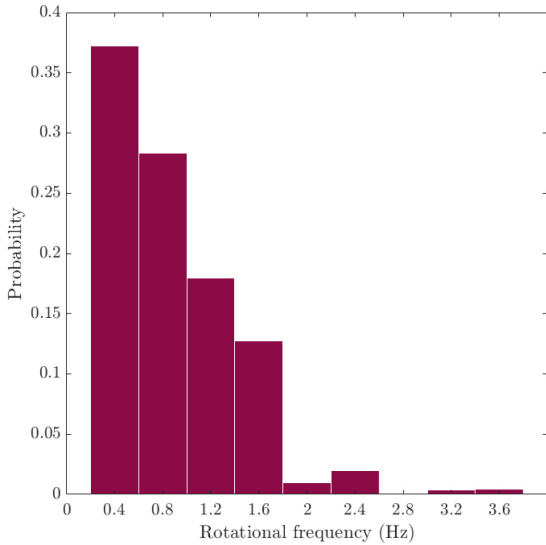
Figure 12. The histogram represents the distribution of the rotational frequency of the whole sample of particles reported in Table 3.
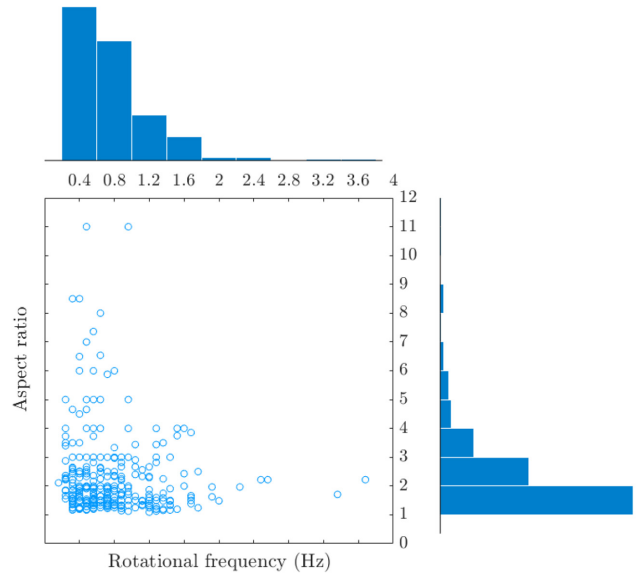

Figure 14. The figure shows the distribution of the particles in the parameter space defined by the particle aspect ratios and the rotational frequencies with their respective histograms.
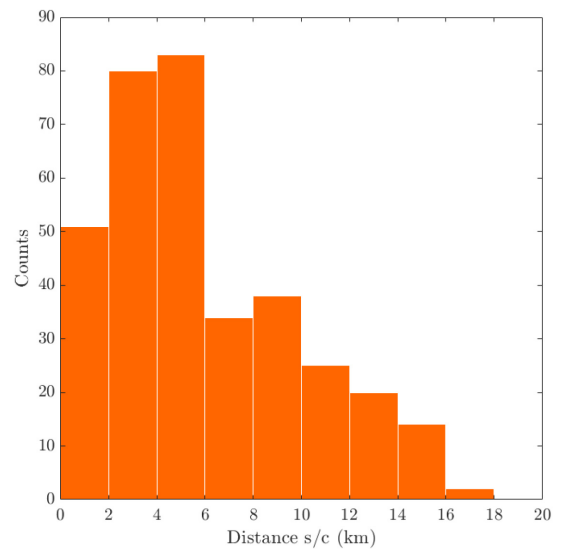

Figure 13. The histogram shows the ellipsoidal particles aspect ratio distribution listed in Table 3.

Figure 15. In the figure the distribution of the particle estimated distances from the spacecraft is shown.

= 1 km. In fact, the smaller is the distance of the particles from the Sun and from the spacecraft and the higher is their radiance. In this way, the possibility to detect a small particle is maximized. We see that the radiance equal to 3×10^{-6} matches to a particle smaller than 1 mm (to which corresponds a radiance equal to 3×10^{-5}) but larger than 0.1 mm (to which corresponds a radiance equal to 3×10^{-7}). Therefore, the particles that we observe in this work are at least of the order of 0.5 mm. This is a lower limit computed in case of particular conditions therefore we expect the majority of the particles to be larger than that limit. The same size range was studied by Ott et al. (2017) who found particles from 1.5×10^{-3} m up to 0.32 m with an average value of 0.05 m. They were able to measure also the speed of those particles, finding that the 90 per cent of them had values between 0 and 5 m s^{-1} with statistic mode equal to 1.25 m s^{-1} (see their fig. 9). The detection of rotating particles is affected by

a bias that facilitates the observation of larger and slower particles. Indeed, very small and faint particles should approach the spacecraft very close to be detected and consequently they would move out of focus. Moreover, particles of the order of 0.1 mm or even smaller, as those measured by GIADA (Della Corte et al. 2015; Rotundi et al. 2015) might reach high velocity and the tracks they generate extend along more pixels with a consequent decrease of intensity that complicates the detection. Therefore, based on the scattering model and on the previous assumptions, we have reasons to think that the tracks observed in these set of images are generated by particles likely larger than 1 mm. Furthermore, the track signal must be high to be able to reveal a brightness variation, thus excluding the fainter particles from the sample. Following this assumption, we use the velocity found by Ott et al. (2017) for particles in the same
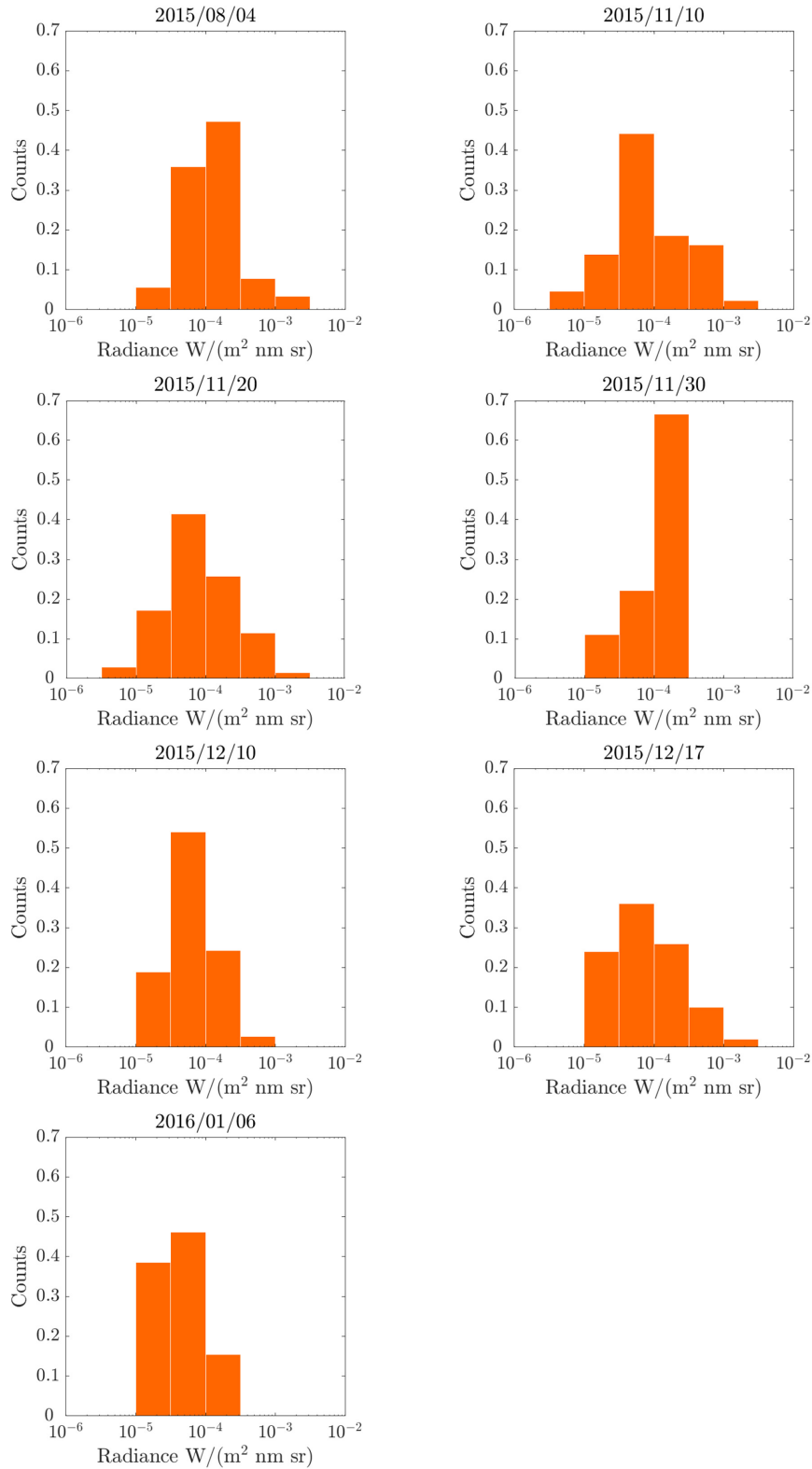
Figure 16. The graphics show the histograms of the dust particle spectral radiances for each epoch from the data set illustrated in Table 3. The sample consists of the same rotating particles analysed in Section 4. The counts are normalized to 1. The spectral radiance is corrected for the phase function and it is in units of W/(m^2 nm sr).

range of size. We approximate the average velocity at which the observed particles move inside the coma with their statistic mode, $v = 1.25 \, \text{m s}^{-1}$. Moreover, we suppose that within the same image the longest tracks represent on average closer particles, while the shorter ones are particles far away from the spacecraft.

The length and the number of rotations depend also on the mass and the size of the particles. We expect that the smallest and lowest density particles reach higher velocity and angular velocity than the large and dense ones (Ivanovski et al. 2017a). In the latter paper, the authors show that this could change if large particles of low density and small particles of high density are studied. In Section 6, we show the results of dust modelling of particles with the same derived dynamical characteristics obtained by this analysis of the observed light curves. Nevertheless, a first investigation can be done, to provide hints about those rotating particles.

We use the length of the tracks to measure the distance of the single particles. In the approximation that the particle velocity distribution mode is a good indicator of the average speed of the observed particles, it is straightforward that the average length covered by a dust particle in 12.5 s of exposure time is of $v \cdot t = 15.625$ m. Therefore, it is possible to construct the following spatial scale: $v \cdot t/l = 15.625/l \, \text{m px}^{-1}$, where l is the length of the tracks in pixel. On the other side, the spatial scale of the NAC camera is $1.86 \, \text{m px}^{-1}$ at 100 km from the spacecraft. Equalling the two scales leads to the following expression:

$$1.86 : 100 = \frac{v \cdot t}{l} : d_{s/c} \qquad (4)$$

from which $d_{s/c}$, the distance of the particles from the spacecraft is immediately computed. The results are shown in Fig. 15, where the histogram represents the average distance distribution. Eventually, the particles analysed in this work, which are observed with the Orange filter at $\lambda = 649$ nm, with an exposure time of 12.5 s seem to reach distance from the spacecraft of less than 20 km.

Ultimately, we compute the size of the rotating particles. We compare the observed values of the spectral radiance of each dust particle with the values obtained with the scattering model at proper heliocentric and spacecraft distances, reported in Appendix B. Each combination of these three parameters (r_h, $d_{s/c}$ and the radiance) corresponds to a specific size. In Fig. 17, we show the parameter space composed by the observed spectral radiances and distances of the dust population listed in Table 3. The distribution of the particles along the line of sight size is shown in Fig. 18. The cm-sized group seems to be the most populated. These results are consistent with the direct measurements of Ott et al. (2017) who found that the bulk of particles has sizes of centimetres.

6 DUST DYNAMICAL SIMULATIONS OF ROTATING NON-SPHERICAL PARTICLES

The 3D + t non-spherical cometary dust model (Fulle et al. 2015; Ivanovski et al. 2017a,b) has been the first one applied to Rosetta data and allowed to obtain those dust physical parameters that were not possible to measure by the on-board instruments due to the operational limitations or instrumental design. First, the model was used in Fulle et al. (2015) to interpret the brightness variation of the tracks in OSIRIS images taken in 2014 October. In this work, we apply the model to data sets of NAC images from 2015 July to 2016 January considering the physical conditions present in 67P coma during this period. We compute the particle rotational frequencies and terminal velocities. We provide a plausible scenario for interpreting the data assuming initial parameters that
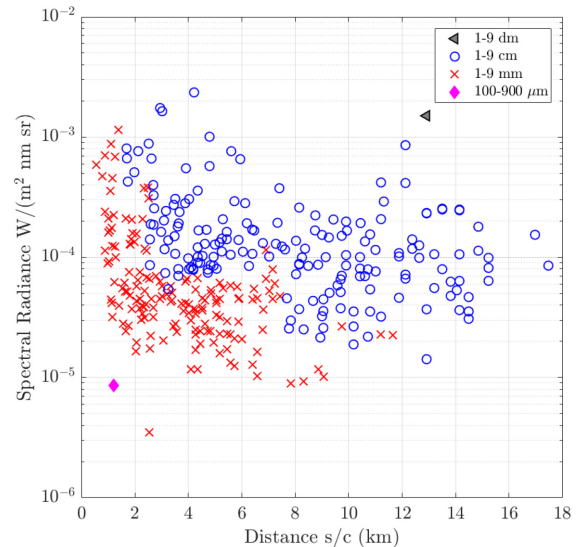

Figure 17. The plot illustrates the distribution of the dust particles in the parameter space defined by their spectral radiances and estimated distances from the spacecraft. The black triangle is a dm-sized particle, the blue circles are the cm-sized particles, the red crosses are the mm-sized particles, and the magenta diamond is a μm-sized particle.
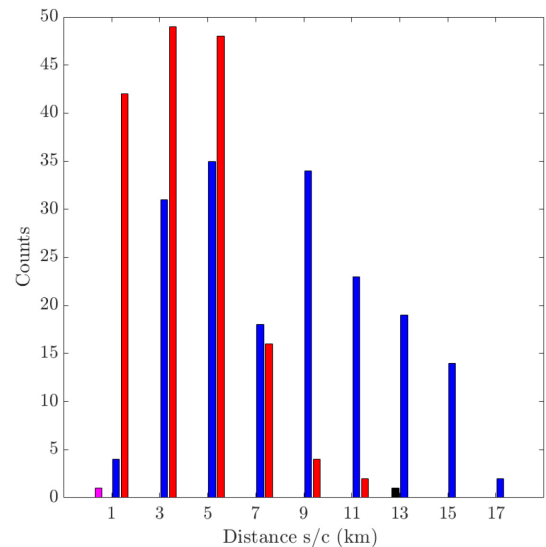

Figure 18. The histogram represents the distribution of the dust particles of different size along the line of sight. The black bars represent the dm-sized particles, the blue ones the cm-sized particles, and the red ones the mm-sized particles.

can lead to the rotational frequencies derived from the observations.

6.1 Model and set-up

We consider homogeneous spheroids with aspect ratio 1.5 – the most probable obtained by the observations in this study. The two main forces acting on the dust particles in closer vicinity to the nucleus are the aerodynamic force and gravity. The analysis of the images show mainly radial outflow (Section 3). We consider that the gas approximation for calculating the aerodynamic force is the Euler one for an expanding ideal gas (Landau & Lifshitz 1987), which is less

time and computationally consuming. The calibration of the physical parameters of these gas solutions is obtained using the GIADA data and the gas production rates reported in Hansen et al. (2016). We shortly review the equations governing the motion of given dust particle:

$$m_d \frac{\mathrm{d}^2 \vec{r}}{\mathrm{d}t^2} = m_d \frac{\mathrm{d}\vec{V}_d}{\mathrm{d}t} = \vec{F}_N + \vec{F}_a$$

$$\vec{F}_N = -G \frac{m_N m_d}{r^3} \vec{r}$$

$$\vec{F}_a = -\int \left(p\vec{n} + \tau \left[(\vec{V}_r \times \vec{n}) \times \vec{n} \right] / |\vec{V}_r \times \vec{n}| \right) \mathrm{d}s, \qquad (5)$$

where $\vec{r}$ and $\vec{V}_d$ are the radius-vector and the velocity of the centre of mass of the particle in the cometocentric non-rotating frame x, y, z; m_d is the particle mass; m_N is the nucleus mass, $\vec{V}_r$ is the gas velocity relative to the elementary surface element of the particle, and $\vec{F}_N$ and $\vec{F}_a$ are the gravity and the aerodynamic forces; p, τ are the gas pressure and the shear stress on the elementary surface element of the particle with area ds (for the exact free molecular expressions, see Shen 2006); $\vec{n}$ is the outward unit vector normal to the elementary surface element, and G is the gravitational constant. Since the minimal collisional mean free path of the gas molecules on the surface is of the order of tens of metres, i.e. much bigger than the considered particle sizes, the flow over the particles may be considered as free molecular (Ivanovski et al. 2017a).

We integrate equations (5) and the Euler dynamical and kinematic equations (for details Landau & Lifshitz 1969) for large distances (Ivanovski et al. 2017b). The gravitational, $\vec{M}_N$, and aerodynamic, $\vec{M}_a$, torques necessary for computing the Euler dynamical equations are given by

$$\vec{M}_N = -\int G m_N \tilde{\rho} \frac{\vec{l}_s \times \vec{r}}{r^3} \mathrm{d}\Gamma$$

$$\vec{M}_a = -\int \vec{l}_s \times \left(p\vec{n} + \tau \left[(\vec{V}_r \times \vec{n}) \times \vec{n} \right] / |\vec{V}_r \times \vec{n}| \right) \mathrm{d}s, \qquad (6)$$

where dΓ is the elementary volume of the particle, $\vec{l}_s$ is the radius-vector towards ds or dΓ from the centre of mass of the particle, and $\tilde{\rho}$ is the dust specific mass.

For the goals of this study, we use the dust parameters constrained by the observations in this paper and the physical parameters of 67P as its mass, gas production, and surface temperature in the considered period. Table 1 summarizes the simulation parameters in two different sets. The first set includes the physical properties of the simulated particles. The second set reviews the 67P measured physical parameters used for the gravity force computation. In particular, we assume a particle bulk density of 800 kg m^{-3} (Fulle et al. 2017) and non-zero initial velocity (see the next subsection). We assume that the particles do not contain any volatiles nor do they fragment, i.e. keep their shape and mass during the whole motion.

6.2 Computed rotational frequencies and particle speeds

We compute the velocities of spheroidal particles with different aspect ratio a/b = 2/3 and 3/2 (oblate and prolate) ranging from b = 0.01 to 1 m. Fig. 19 shows the computed particle velocities and rotational frequencies of spheroids of the same size (b = 1 cm) and density (800 kg m^{-3}) as found as the most probable candidates derived in the present study from the analysis of the OSIRIS data. These velocities and rotation frequencies are close to those in Ivanovski et al. (2017b) found for particles of the same size, moving in the same gas field, but with density 1000 kg m^{-3} and a/b = 2.0. In

the present simulations the gas production rate is 100 times greater than used in Fulle et al. (2015) (due to the variation of the gas production from pre-landing period in 2014 October to perihelion in 2015 August). The results show that the considered particles remain slow rotators (<0.01 Hz).

Fig. 12 shows that the majority of the observed particles have frequency ~0.4 Hz. The most brightness frequency in 2014 October data was 0.3 Hz, while during and post-perihelion it is 0.4 Hz. If we compute the most probable rotational frequency considering both the shorter exposure time 12.5 s [~2/3 of the one used in the measurements during 2014 October 12–13 and 19–20 (fig. 4, Fulle et al. 2015)] and the most probable frequency of those periods i.e. ~0.3, we obtain as a most probable frequency ~0.4 i.e. the same as the one derived in our measurements analysis. The latter fact evidences that the most probable rotational frequency has not changed when approaching the Sun.

Since the perihelion data analysis cannot disentangle the prolate of oblate shapes, we perform simulations for both shapes, i.e. a/b = 2/3 and 3/2. The oblate particle obtain higher rotational frequency than the prolate particle, but it is still lower than derived from the observations. Among the possible explanations could be uncertainty of the particle detachment process (i.e. presence of initial velocity and/or torque and/or rocket force due to particle sublimation). Therefore, we perform simulations for these spheroids assuming that they have initial velocity which corresponds to the maximum possible ejection velocity of a particle with the same volume and mass estimated for 67P nucleus in Fulle et al. (2020) (assuming complete transfer of the gas thermal energy at the detachment into the initial kinetic energy of the particle). This initial velocity is of few centimetres per second and does not affect the resulting rotational motion in our simulations. Owing to the large uncertainty in the values to be adopted for the initial torque and possible outgassing from the particle we do not try to address this in the current work. A preliminary study shows that the high initial rotational frequencies (>0.4 Hz) can remain unchanged during the particle motion through the coma.

7 SUMMARY AND CONCLUSIONS

In this work, we have analysed a collection of images of the inner coma of the comet 67P/Churyumov–Gerasimenko with the aim of describing the physical and dynamical properties of the single dust particles to provide constraints for theoretical 3D coma models.

In Section 3, we performed a dynamical analysis of the particles in the inner coma of 67P. We measured the direction of motion directly from the images revealing highly radial trajectories with respect to the nucleus. This suggested that the material originated from the nucleus and that all deviations from the radiality might be interpreted as a small population of bound orbiting objects.

In Section 4, we focused on a group of particles that showed evidence of rotational motion. The sample represented about the 18 per cent of the whole population, while the remaining showed homogeneously bright tracks. We measured a rotational frequency with a decreasing trend up to a maximum value of $\nu = 3.6 \pm 0.2$ Hz. It was not possible to detect particles with values of rotational frequency below 0.24 Hz since the exposure time of the images was not long enough to identify slow rotating objects. The decreasing trend of the frequency distribution and the fact that the sample represented only a small part of the overall dust particles population suggested that the majority of them rotated slower than the group studied in this work. Consequently, no fragmentation of the aggregates was expected. The light curves analysis provided also the aspect ratio of
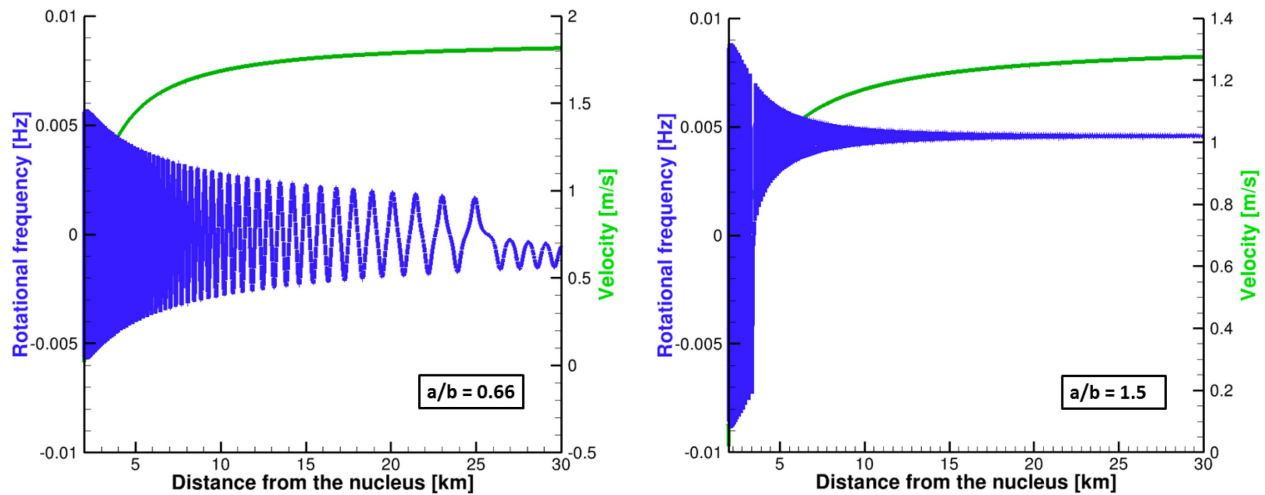
Figure 19. Particle velocity (green lines) and rotational frequencies(blue lines) in two cases: spheroid with aspect ratio $a/b = 0.66$ (left) and spheroid with aspect ratio $a/b = 1.5$ (right). Both spheroids are with size $b = 1$ cm in radius and bulk density 800 kg m^{-3} is considered. The complete list of the particle parameters are given in Table 1.

the single dust particles in the approximation of ellipsoidal shape, contributing to characterize them. The majority of the population had values that range between 1 and 2, revealing a moderate level of flattening. Nevertheless, the aspect ratio reached values quite high, up to 11, revealing the particles might be also very elongated.

In Section 5, we performed the photometric analysis of the same samples of particles used in the previous section. We measured their fluxes and by comparing them with simulated ones we derived their size. We took into account two types of composition, i.e. silicates and organic, and we computed the radiance produced by different sizes at different distances from the camera with a Mie scattering model. The direct comparison of the simulated fluxes with the observed ones provided a size distribution of the particles that ranged from the value of millimetres up to the decimetres. Following those calculations, it seemed that the camera was not able to detect particles smaller than millimetres (except one case of a particle of the order of 0.1 mm) since they should have had a flux fainter than the background.

These observational measurements worked as constraints for the theoretical dynamical model used in Section 6 to compute the velocity and rotational frequencies of the dust particles. The results of the simulation showed that particles with the same characteristics of the observed ones remained slow rotators ($\nu < 0.01$ Hz). Therefore, the simulations confirmed that the majority of the particle population should have had a low rotational frequency. The explanation to characterize the motion of the fast-rotating particles still misses. A possible hint could be related with the uncertainty of the particle detachment processes that might transmit them an initial rotational velocity.

DATA AVAILABILITY

All the data underlying this paper are available at https://www.cosmos.esa.int/web/psa/rosetta.

REFERENCES

Acton C. H., 1996, Planet. Space Sci., 44, 65
Bardyn A. et al., 2017, MNRAS, 469, S712
Bertini I. et al., 2017, MNRAS, 469, S404
Bertini I. et al., 2019, MNRAS, 482, 2924
Colangeli L. et al., 2007, Space Sci. Rev., 128, 803
Crifo J. F., Lukianov G. A., Rodionov A. V., Khanlarov G. O., Zakharov V. V., 2002, Icarus, 156, 249

Crifo J.-F., Loukianov G. A., Rodionov A. V., Zakharov V. V., 2005, Icarus, 176, 192

Della Corte V. et al., 2014, J. Astron. Instrum., 3, 1350011

Della Corte V. et al., 2015, A&A, 583, A13

Della Corte V. et al., 2016, MNRAS, 462, S210

Frattin E. et al., 2017, MNRAS, 469, S195

Frattin E. et al., 2019, MNRAS, 484, 2198

Fray N. et al., 2017, MNRAS, 469, S506

Fulle M., Blum J., 2017, MNRAS, 469, S39

Fulle M. et al., 2015, A&A, 583, A14

Fulle M. et al., 2016a, MNRAS, 462, S132

Fulle M. et al., 2016b, ApJ, 821, 19

Fulle M. et al., 2017, MNRAS, 469, S45

Fulle M., Blum J., Rotundi A., Gundlach B., Güttler C., Zakharov V., 2020, MNRAS, 493, 4039

Güttler C. et al., 2019, A&A, 630, A24

Hansen K. C. et al., 2016, MNRAS, 462, S491

Ivanovski S. L., Zakharov V. V., Della Corte V., Crifo J.-F., Rotundi A., Fulle M., 2017a, Icarus, 282, 333

Ivanovski S. L. et al., 2017b, MNRAS, 469, S774

Keller H. U. et al., 2007, Space Sci. Rev., 128, 433

Landau L. D., Lifshitz E. M., 1969, Mechanics, Course of Theoretical Physics, Oxford: Pergamon Press

Landau L. D., Lifshitz E. M., 1987, Fluid Mechanics, Pergamon, Oxford

Langevin Y. et al., 2016, Icarus, 271, 76

Le Roy L., Bardyn A., Briois C., Cottin H., Fray N., Thirkell L., Hilchenbach M., 2015, Planet. Space Sci., 105, 1

Mannel T., Bentley M. S., Schmied R., Jeszenszky H., Levasseur-Regourd A. C., Romstedt J., Torkar K., 2016, MNRAS, 462, S304

Marschall R. et al., 2016, A&A, 589, A90

Moreno F. et al., 2017, MNRAS, 469, S186

Moreno F. et al., 2018, AJ, 156, 237

Muñoz O., Volten H., de Haan J. F., Vassen W., Hovenier J. W., 2000, A&A, 360, 777

Muñoz O. et al., 2020, ApJS, 247, 19

Ott T. et al., 2017, MNRAS, 469, S276

Pätzold M. et al., 2016, Nature, 530, 63

Riedler W. et al., 2007, Space Sci. Rev., 128, 869

Rotundi A., Ferrini G., Baratta G. A., Palumbo M. E., Palomba E., Colangeli L., 2007, Dust Planet. Syst., 643, 149

Rotundi A. et al., 2008, Meteorit. Planet. Sci., 43, 367

Rotundi A. et al., 2015, Science, 347, aaa3905

Shen C., 2006, Rarefied Gas Dynamics: Fundamentals, Simulations and Micro Flows, Heat and Mass Transfer. Springer, Berlin, Heidelberg

Sierks H. et al., 2015, Science, 347, aaa1044

Skorov Y., Reshetnyk V., Lacerda P., Hartogh P., Blum J., 2016, MNRAS, 461, 3410

Skorov Y., Reshetnyk V., Rezac L., Zhao Y., Marschall R., Blum J., Hartogh P., 2018, MNRAS, 477, 4896

Tubiana C. et al., 2015, A&A, 583, A46

Wolf S., Voshchinnikov N. V., 2004, Comput. Phys. Commun., 162, 113

Zakharov V. V., Rodionov A. V., Lukianov G. A., Crifo J. F., 2009, Icarus, 201, 358

Zakharov V. V., Ivanovski S. L., Crifo J. F., Della Corte V., Rotundi A., Fulle M., 2018, Icarus, 312, 121

APPENDIX A: TRANSLATIONAL MOTION OF THE DUST
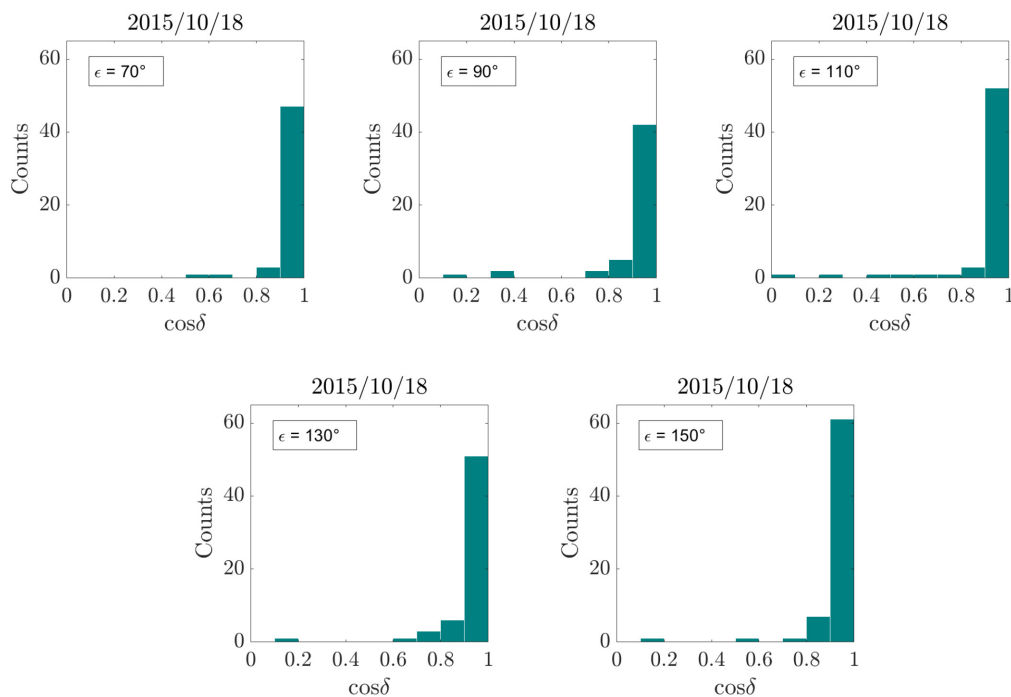
Figure A1. The histograms show the value of the cosine of the angle δ between the velocity vector of the particle on the image plane, and the projected position vector of the nucleus on the plane of the image, in the NAC reference system, for the set STP 078 GRAIN_COLOR_004.
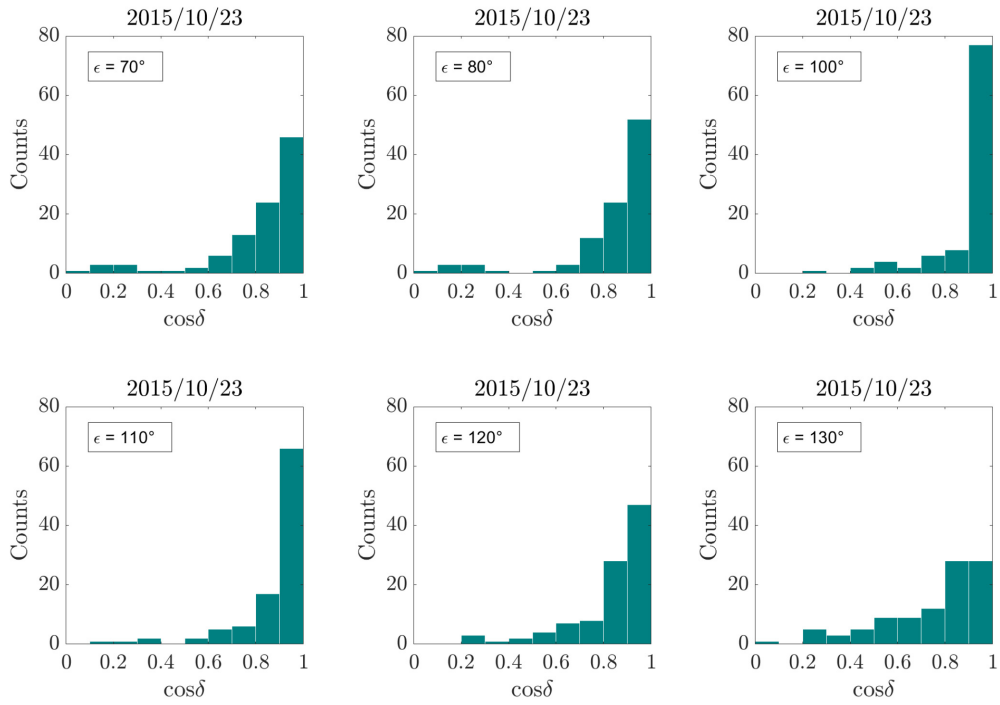
Figure A2. The histograms show the value of he cosine of the angle δ for the set STP 079 GRAIN_COLOR_001.
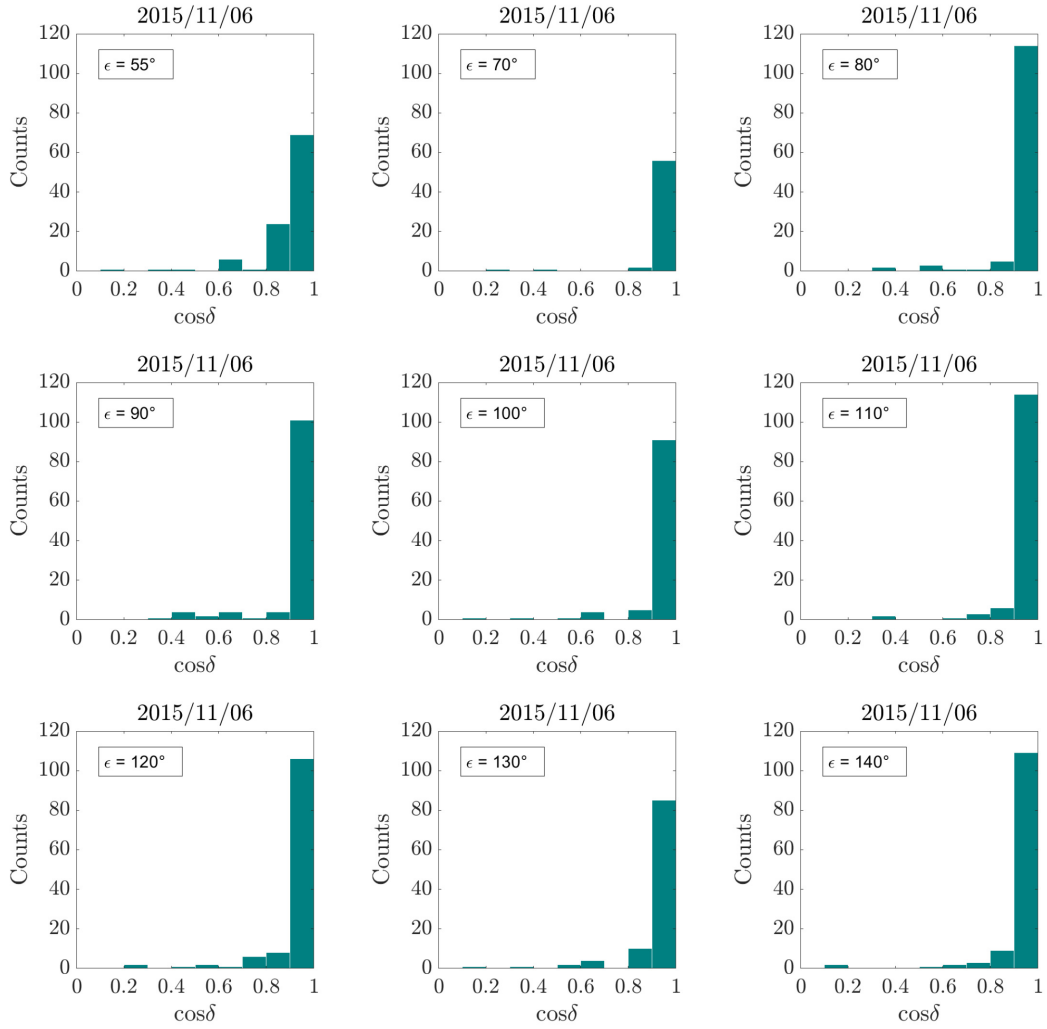
Figure A3. The histograms show the value of the cosine of the angle δ for the set STP 081 GRAIN_COLOR_002.
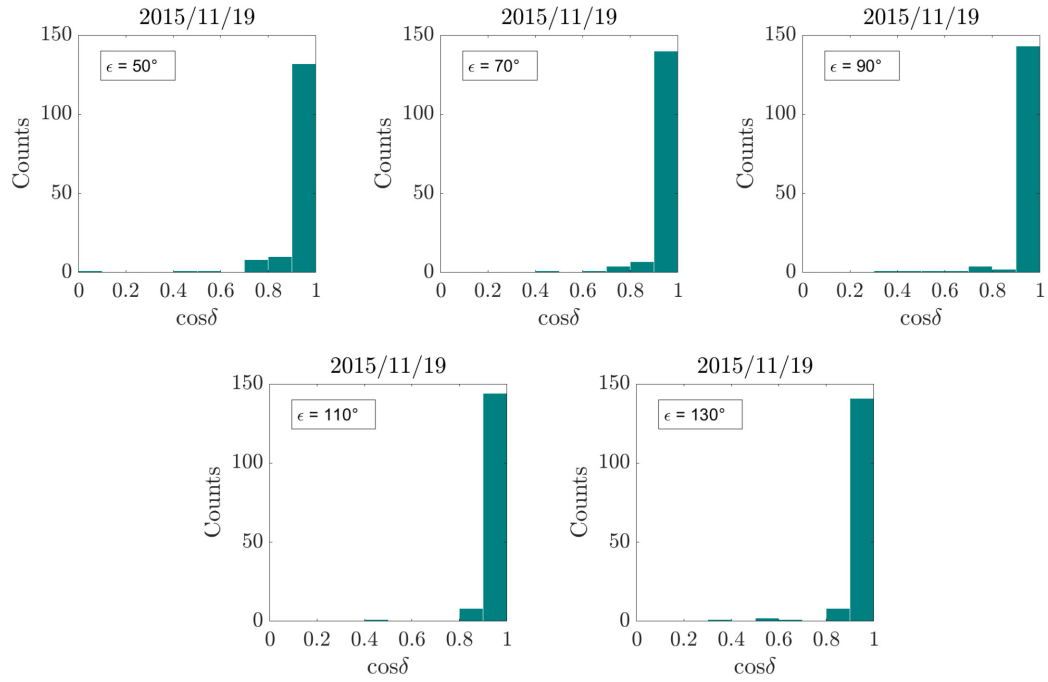
Figure A4. The histograms show the value of the cosine of the angle δ for the set STP 083 GRAIN_COLOR_001.

APPENDIX B: SCATTERING SIMULATIONS

Table B1. In this table, we report the expected spectral radiance of a dust particle, for different combinations of the scattering code parameters. r_h: the heliocentric distance, a: the size of the particles, $d_{s/c}$: the distance of the particle from the spacecraft. Silicates and Organics Radiance are in units of W/(m^{2}nm sr). The refractive index of the silicate material is $m = 1.6 + i10^{-5}$, and the refractive index of the organic material is $m = 1.3 + i10^{-2}$.

r_h (au)	a (mm)	$d_{s/c}$ (km)	Silicates radiance	Organics radiance
1.3	0.1	1	8.2×10^{-7}	3.0×10^{-7}
		2	2.1×10^{-7}	7.5×10^{-8}
		5	3.3×10^{-8}	1.2×10^{-8}
		10	8.2×10^{-9}	3.0×10^{-9}
		15	3.7×10^{-9}	1.3×10^{-9}
		20	2.1×10^{-9}	7.5×10^{-9}
1.3	1	1	1.0×10^{-4}	3.0×10^{-5}
		2	2.5×10^{-5}	7.5×10^{-6}
		5	4.0×10^{-6}	1.2×10^{-6}
		10	1.0×10^{-6}	3.0×10^{-7}
		15	4.4×10^{-7}	1.3×10^{-7}
		20	2.5×10^{-7}	7.5×10^{-8}
1.3	10	1	7.6×10^{-3}	2.9×10^{-3}
		2	1.9×10^{-3}	7.3×10^{-4}
		5	3.0×10^{-4}	1.2×10^{-4}
		10	7.6×10^{-5}	2.9×10^{-5}
		15	3.4×10^{-5}	1.3×10^{-5}
		20	1.9×10^{-5}	7.3×10^{-6}
1.7	0.1	1	4.8×10^{-7}	1.8×10^{-7}
		2	1.2×10^{-7}	4.5×10^{-8}
		5	1.9×10^{-8}	7.2×10^{-9}
		10	4.8×10^{-9}	1.8×10^{-9}
		15	2.1×10^{-9}	8.0×10^{-10}
		20	1.2×10^{-9}	4.5×10^{-10}
1.7	1	1	5.8×10^{-4}	1.8×10^{-5}
		2	1.5×10^{-5}	4.5×10^{-6}
		5	2.3×10^{-6}	7.2×10^{-7}
		10	5.8×10^{-7}	1.8×10^{-7}
		15	2.6×10^{-7}	8.0×10^{-8}
		20	1.5×10^{-7}	4.5×10^{-8}
1.7	10	1	4.5×10^{-3}	1.8×10^{-3}
		2	1.1×10^{-3}	4.0×10^{-4}
		5	1.8×10^{-4}	7.0×10^{-5}
		10	4.5×10^{-5}	1.8×10^{-5}
		15	2.0×10^{-5}	7.8×10^{-6}
		20	1.1×10^{-5}	4.4×10^{-6}
2.0	0.1	1	3.5×10^{-7}	1.3×10^{-7}
		2	8.8×10^{-8}	3.3×10^{-8}
		5	1.4×10^{-9}	5.2×10^{-9}
		10	3.5×10^{-9}	1.3×10^{-9}
		15	1.5×10^{-9}	5.8×10^{-10}
		20	8.8×10^{-10}	3.3×10^{-10}
2.0	1	1	4.2×10^{-5}	1.3×10^{-5}
		2	1.1×10^{-5}	3.3×10^{-6}
		5	1.7×10^{-6}	5.2×10^{-7}
		10	4.2×10^{-7}	1.3×10^{-7}
		15	1.9×10^{-7}	5.8×10^{-8}
		20	1.1×10^{-8}	3.3×10^{-8}
2.0	10	1	3.2×10^{-3}	1.3×10^{-3}
		2	8.0×10^{-4}	3.2×10^{-4}
		5	1.3×10^{-4}	5.2×10^{-5}
		10	3.2×10^{-5}	1.3×10^{-5}
		15	1.4×10^{-5}	5.7×10^{-6}
		20	8.0×10^{-6}	3.3×10^{-6}

This paper has been typeset from a TEX/LATEX file prepared by the author.